

Supporting Information

Exponential Amplification by Redox Cross-Catalysis and Unmasking of Doubly Protected Molecular Probes

Justine Pallu, Charlie Rabin, Pan Hui, Thamires S. Moreira, Geordie Creste, Corentin Calvet,
Benoît Limoges,* François Mavré,* and Mathieu Branca*

Université de Paris, Laboratoire d'Electrochimie Moléculaire, UMR 7591, CNRS, F-75013 Paris, France

Table of Content

1. Experimental Section.....	3
1.1. <i>Material and methods</i>	3
1.2. <i>Chemical synthesis</i>	3
2. Influence of pH on the autocatalysis rate of P₂.....	6
3. UV-vis spectrophotometric characterization of P₂ stability and evolution in either the presence or absence of O₂ or H₂O₂.	7
4. HPLC analysis of the time course evolution of P₂ in a Tris buffer	7
5. Kinetic analysis of the H₂O₂-mediated deprotection of P₂.....	9
6. UV-vis spectrophotometric characterization of P₃ either in the absence or presence of H₂O₂.	10
7. Kinetic analysis of the H₂O₂-mediated deprotection of P₃.....	11
8. Autocatalytic reaction scheme involving P₃ and NADH/diaphorase and its numerical simulations	12
9. Justification of the rate constants used in the autoxidation mechanism of 1,4-NQ	13
10. Determination of the enzyme rate constants k_3 and k_{red} from redox cycling experiments with 1,4-NQ and their analysis by numerical simulations	14
11. Numerical simulation of the autocatalysis with P₂.....	16
12. Influence of the buffer nature and pH on the autocatalytic reaction with P₃.....	17
12.1. <i>Tris buffer (pK_a = 8.1)</i>	17
12.2. <i>Bicine buffer (pK_a = 8.3)</i>	18
12.3. <i>CAPSO buffer (pK_a = 9.6)</i>	19
12.4. <i>CHES buffer (pK_a = 9.3)</i>	20
12.5. <i>Borate buffer (pK_a = 9.3)</i>	21
12.6. <i>Glycine buffer (pK_a = 9.6)</i>	22
12.7. <i>Carbonate buffer (pK_a = 10.3)</i>	23
12.8. <i>CAPS buffer (pK_a = 10.4)</i>	24
13. Screening of naphthoquinones for their redox cycling properties.	25
14. UV-vis spectrophotometric characterization of P₄ (either in the absence or presence of H₂O₂) and 2-MeO-NQ.....	26
15. Indirect detection of glucose oxidase (GOD)	26
16. References.....	27

1. Experimental Section

1.1. Material and methods

All chemicals for synthesis were purchased either from Sigma-Aldrich, Fischer Scientific or TCI Europe and used without further purification unless specified. Bicine (99%), glycine (99%), NADH, and 2-amino-3-chloro-1,4-naphthoquinone (2-A-3-Cl-1,4-NQ, 97+%) were purchased from TCI. Trizma® base (minimum 99.9% titration), N-cyclohexyl-3-aminopropanesulfonic acid (CAPS, 98%), 3-(cyclohexylamino)-2-hydroxy-1-propanesulfonic acid (CAPSO, 99%), sodium carbonate (99.5%), HCl (97%), sodium tetraborate (99%), N-Cyclohexyl-2-aminoethanesulfonic acid (CHES, 99%), EDTA (99.999%), DMSO (anhydrous $\geq 99.9\%$), menadione (98%), 2,3-dichloro-1,4-naphthoquinone (2,3-diCl-1,4-NQ, 98%), 2-methoxy-1,4-naphthoquinone (2-MeO-1,4-NQ, 98%), 1,2-naphthoquinone (1,2-NQ, 97%), 2-hydroxy-1,4-naphthoquinone (2-OH-1,4-NQ, 97%) were obtained from Sigma-Aldrich/Merk. The 1,4-naphthoquinone (1,4-NQ, 97%) from Janssen was recrystallized before used. Hydrogen peroxide for analysis (35 wt.% in water) and D(+)-glucose was acquired from Acros Organics. Lyophilized diaphorase I from *Bacillus stearothermophilus* (DI, EC 1.6.99.-) was obtained from Nipro (Japan). Before use, the mother solution of DI was centrifuged ($11000 \times g$, 30 min, 4°C) over a Nanosep membrane of 10 kDa molecular weight cut-off (Pall Corporation) pre-equilibrated with a PBS Buffer.

Flash chromatographies were performed on Kieselgel 60 (35–70 μm) silica gel. ^1H and ^{13}C NMR spectra were recorded on a Bruker AC 400 MHz and were measured using CDCl_3 , CD_3OD , CD_3CN , Acetone- d_6 , DMSO- d_6 or DMF- d_7 as solvent. Multiplicities in NMR spectra are reported as follows: s = singlet, d = doublet, t = triplet, sept = septuplet, m = multiplet, bs = broad singlet, bd = broad doublet. Chemical shifts are reported in δ units to 0.01 ppm precision for ^1H and 0.1 ppm for ^{13}C using residual solvent as an internal reference. Mass spectra were measured on a MAT95S Finnigan-Thermo spectrometer.

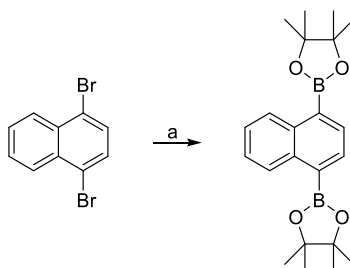
The mother solutions of each of the boronic ester probes (50 mM) were prepared in pure DMSO (Fluka) and stored in the fridge no more than 2–3 days. Concentrated solutions of hydrogen peroxide and NADH were daily prepared in Milli-Q water before then to be diluted at the desired concentrations in the desired buffer. Unless otherwise stated, a 0.1 M Tris-EDTA buffer of pH 8.5 (prepared from Trizma® base and HCl) and containing 10 μM EDTA was used.

For the standard spectrophotometric measurements, a UV/Vis spectrophotometer Specord S600 from Analytical Jena (Jena, Germany) in quartz cuvette of 1-cm optical path-length was employed, while for the high throughput UV-vis absorbance kinetic experiments, a Spark® multimode microplate reader (Tecan, Switzerland) with a standard Nunc 96-well UV transparent, clear flat-bottom microplate (Thermo Fisher) was used. The autocatalytic reactions triggered by H_2O_2 in the microplate were achieved by rapidly mixing 100 μL of solutions containing probe (100 μM), NADH (500 μM) and DI (either 20 nM or 0.2 nM) to 100 μL of H_2O_2 solutions at different concentrations beforehand distributed throughout the wells (the final concentrations of the species being thus divided by 2), and then the microplate immediately scanned by UV-vis spectrophotometry every 10 s. The same procedure was used for the autocatalytic reactions triggered by the 2-amino-3-chloro-1,4-NQ. Autocatalytic reactions triggered by the glucose oxidase were achieved by rapidly mixing 100 μL of glucose oxidase solutions at different concentrations to 100 μL of solutions containing probe (100 μM), DI (0.2 nM), NADH (500 μM), and glucose (100 mM) in advance distributed throughout the wells. All experiments were done in triplicate in an air-conditioned room maintained at a temperature of $25^\circ\text{C} \pm 2^\circ\text{C}$. Also during the whole reaction, the microplates were left open to the air. From the calibration plots, the LOD was determined as three time the standard deviation of the blank response.

For the numerical simulations of kinetics, the COPASI freeware was used (version 4.16).^{S1}

1.2. Chemical synthesis

Synthesis of 1,4-bis(4,4,5,5-tetramethyl-1,3,2-dioxaborolan-2-yl)naphthalene (probe P₃). The synthesis was carried out as depicted in Scheme S1 by following a described procedure starting from the 1,4-dibromonaphthalene.^{S2}



Scheme S1. Synthesis of P₃. a) Bis(pinacolato)diboron (3 eq.), $\text{PdCl}_2(\text{CH}_3\text{CN})_2$ (0.14 eq.), dppf (0.14 eq.), AcOK (6 eq.), 1,4-dioxane, 100°C , 24h, 71%.

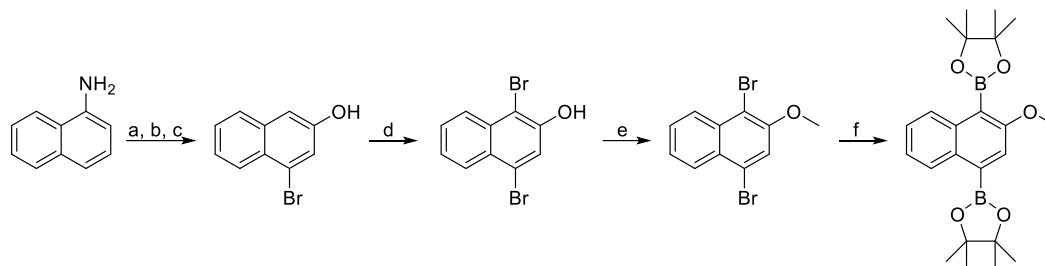
The product was further purified by recrystallization from *n*-hexane to yield 667 mg of **P₃** (71%).

¹H NMR (400 MHz, CDCl₃): δ (ppm) = 8.73 (dd, *J* = 3.4 and 6.5 Hz, 2H), 8.01 (s, 2H), 7.50 (dd, *J* = 3.4 and 6.5 Hz, 2H), 1.41 (s, 24H).

¹³C NMR (100 MHz, CDCl₃): δ (ppm) = 136.8 (C_{qAr}), 134.5 (C_{HAr}), 130.9 (C_{qAr}, deduced from HMBC), 128.8 (C_{HAr}), 126.0 (C_{HAr}), 84.0 (C_q), 25.2 (C_H)

HRMS (*m/z*): Calculated (C₂₂H₃₀B₂NaO₄): 403.221414. Found: 403.22302.

Synthesis of 1,4-bis(4,4,5,5-tetramethyl-1,3,2-dioxaborolan-2-yl)-2-methoxynaphthalene (probe **P₄).** The synthesis of **P₄** was carried out according to the sequential reaction steps reported in Scheme S2.



Scheme S2. Synthesis of **P₄**. a) Br₂ (2.2 eq.), AcOH, 0°C, 15 min then 60°, 15 min; 99% b) NaNO₂ (1.02 eq.), AcOH, EtCO₂H, 0°C, 10 min, 65% c) NaBH₄ (1.02 eq.), EtOH, 0°C, 3h, 99%; d) NBS (1 eq.), CH₃CN, 0°C, 3h, 92%; e) Me₂SO₄ (2 eq.); K₂CO₃ (2eq.), acetone, RT°, overnight, 38%; f) Bis(pinacolato)diboron (3 eq.), PdCl₂(CH₃CN)₂ (0.14 eq.), dppf (0.14 eq.), AcOK (6 eq.), DMF, 110°C, 37h, 32%.

4-bromonaphthalen-2-ol. The synthesis was carried out by following a described procedure^{S3} starting from 1-naphthylamine (5 g) to yield 5 g of the expected product (64%).

¹H NMR (400 MHz, CDCl₃): δ (ppm) = 8.11 (dd, *J* = 1.5 and 7.5 Hz, 1H), 7.64 (dd, *J* = 1.5 and 7.5 Hz, 1H), 7.48-7.37 (m, 3H), 7.12 (d, *J* = 2.4 Hz, 1H), 5.12 (broad, 1H).

1,4-dibromonaphthalen-2-ol. A NBS (1.79 g, 10.06 mmol) solution in CH₃CN (25 mL) was added dropwise over 45 min and at 0°C to a solution of 4-bromonaphthalen-2-ol (1.83 g, 8.20 mmol) in CH₃CN (25 mL). Stirring was continued at RT° for 2h. 50 mL of water is then added to the reaction media and the resulting solution was extracted three times with diethyl ether. The organic phase is washed successively with a NaHCO₃ 5% wt. solution and a 1N HCl solution and is then dried over Na₂SO₄. The organic phase is filtered and the solvents evaporated to yield 2.27g of crude 1,4-dibromonaphthalen-2-ol which was directly used in the next step without further purification.

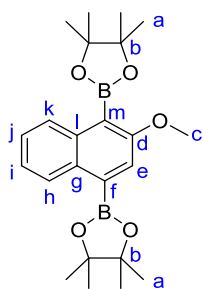
¹H NMR (400 MHz, CDCl₃): δ (ppm) = 8.19 (dd, *J* = 1.4 and 7.9 Hz, 1H), 7.84 (dd, *J* = 1.4 and 7.9 Hz, 1H), 7.69 (broad, 1H), 7.56 (ddd, *J* = 1.4, 7.7 and 7.9 Hz, 1H), 7.47 (ddd, *J* = 1.4, 7.7 and 7.9 Hz, 1H), 6.94 (s, 1H).

1,4-dibromo-2-methoxynaphthalene. Me₂SO₄ (1.43 mL, 15.06 mmol) was added to a 35 mL solution of K₂CO₃ (2.08 g, 15.06 mmol) and 1,4-dibromonaphthalen-2-ol (2.27 g, 7.529 mmol) in acetone at RT°. The reaction is stirred for 5h at RT°. After completion of the reaction as checked by TLC (Hexane/AcOEt:95/5) the solvent is evaporated and the crude compound is purified by flash chromatography with petroleum ether yielding 900 mg (38%) of pure 1,4-dibromo-2-methoxynaphthalene.

¹H NMR (400 MHz, CDCl₃): δ (ppm) = 8.24 (dd, *J* = 1.3 and 8.3 Hz, 1H), 8.14 (dd, *J* = 1.3 and 8.3 Hz, 1H), 7.58 (ddd, *J* = 1.3, 6.8 and 8.3 Hz, 1H), 7.58 (s, 1H), 7.48 (ddd, *J* = 1.3, 6.8 and 8.3 Hz, 1H), 4.01 (s, 3H).

¹³C NMR (100 MHz, CDCl₃): δ (ppm) = 153.6 (C_q), 133.8 (C_q), 128.7 (C_H), 128.5 (C_q), 128.8 (C_H), 127.7 (C_H), 126.9 (C_H), 125.9 (C_H), 123.4 (C_q), 118.1 (C_H), 108.8 (C_q), 57.5 (C_{CH3}).

1,4-bis(4,4,5,5-tetramethyl-1,3,2-dioxaborolan-2-yl)-2-methoxynaphthalene. In a dry schlenk tube and under an argon atmosphere were dissolved 1,4-dibromo-2-methoxynaphthalene (400 mg, 1.26 mmol), dry potassium acetate (744 mg, 7.58 mmol) and bis(pinacolato)diboron (964 mg, 3.79 mmol) in 13.6 mL of anhydrous DMF. Argon was bubbled in the reaction medium for 15 min then bis(acetonitrile)palladium dichloride (45.7 mg, 0.176 mmol) and 1,1'-bis(diphenylphosphino)ferrocene (97.6 mg, 0.176 mmol) were added and the bubbling was continued for 10 min. The reaction medium was then heated at 110°C for 37h and was then diluted in ethyl acetate, filtered on celite and the solvent was evaporated. The crude product was directly purified by flash chromatography (pentane/diethyl ether: 95/5→80/20) yielding 164 mg of **P₄** as a white powder (32%). Samples of higher purity were obtained by recrystallization from *n*-hexane (73mg, 45% recrystallization yield).



^1H NMR (400 MHz, CDCl_3): δ (ppm) = 8.65 (dd, J = 1.4 and 8.2 Hz, 1H_h), 7.82 (dd, J = 1.4 and 8.2 Hz, 1H_k), 7.73 (s, 1H_e), 7.38 (ddd, J = 1,4, 6.8 and 8.2 Hz, 1H), 7.32 (ddd, J = 1,4, 6.8 and 8.2 Hz, 1H), 3.93 (s, 3H_c), 1.45 (s, 12H_a), 1.40 (s, 12H_a).

^{13}C NMR (100 MHz, CDCl_3): δ (ppm) = 160.5 (C_d), 137.4 (C_m), 132.8 (C_f), 132.5 (C_l , deduced from HMBC), 128.8 (C_h), 127.4 (C_k), 126.2 (C_i), 124.0 (C_j), 122.1 (C_e), 118.5 (C_g deduced from HMBC), 84.2 (C_b), 84.1 (C_b), 57.1 (C_c), 25.2 (C_a), 25.2 (C_a).

HRMS (m/z): Calculated ($\text{C}_{23}\text{H}_{32}\text{B}_2\text{NaO}_5$): 433.232117. Found: 433.233624.

2. Influence of pH on the autocatalysis rate of P₂

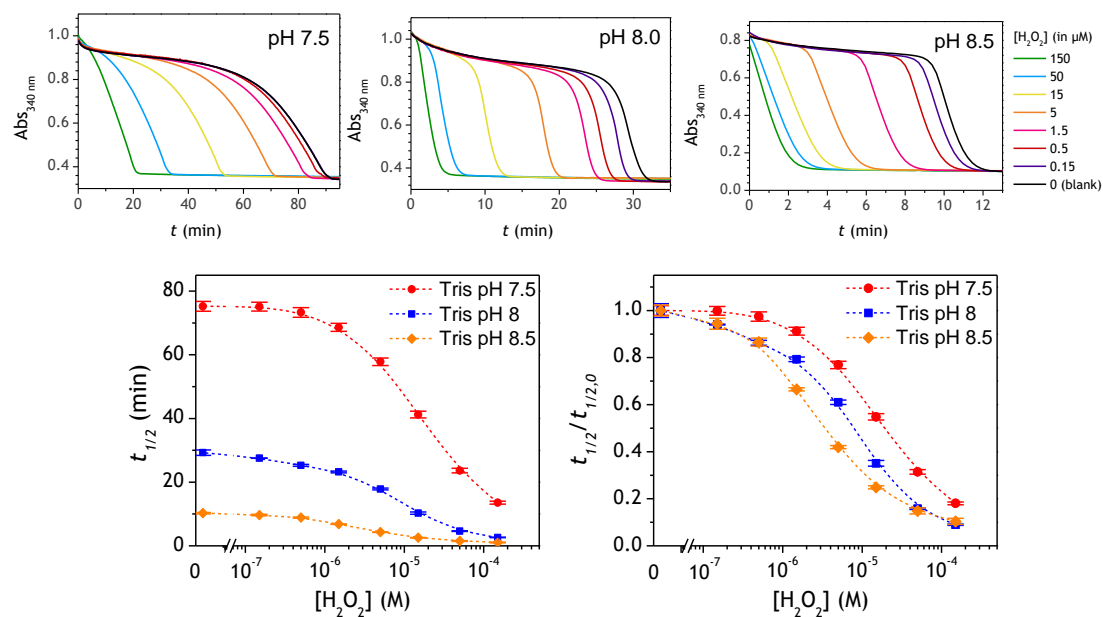


Figure S1. (Top) UV-vis kinetic traces monitored at 340 nm immediately after the injection of different concentrations of H₂O₂ (as indicated in the caption on the right) to solutions containing 50 μM P₂, 10 nM DI and 250 μM NADH. All experiments were conducted in air-saturated Tris buffers (0.1 M) containing 10 μM EDTA. The pH of buffer is as indicated on the graphs. Each curve is the average of triplicate experiments. (Bottom) Semi-logarithmic calibration curves obtained from the plot of $t_{1/2}$ as a function of H₂O₂ concentration. For the normalized plots on the right, the $t_{1/2}$ values were divided by the blank threshold time determined in the absence of H₂O₂ (i.e., $t_{1/2,0}$). Errors bars are standard deviations from triplicates.

3. UV-vis spectrophotometric characterization of P_2 stability and evolution in either the presence or absence of O_2 or H_2O_2 .

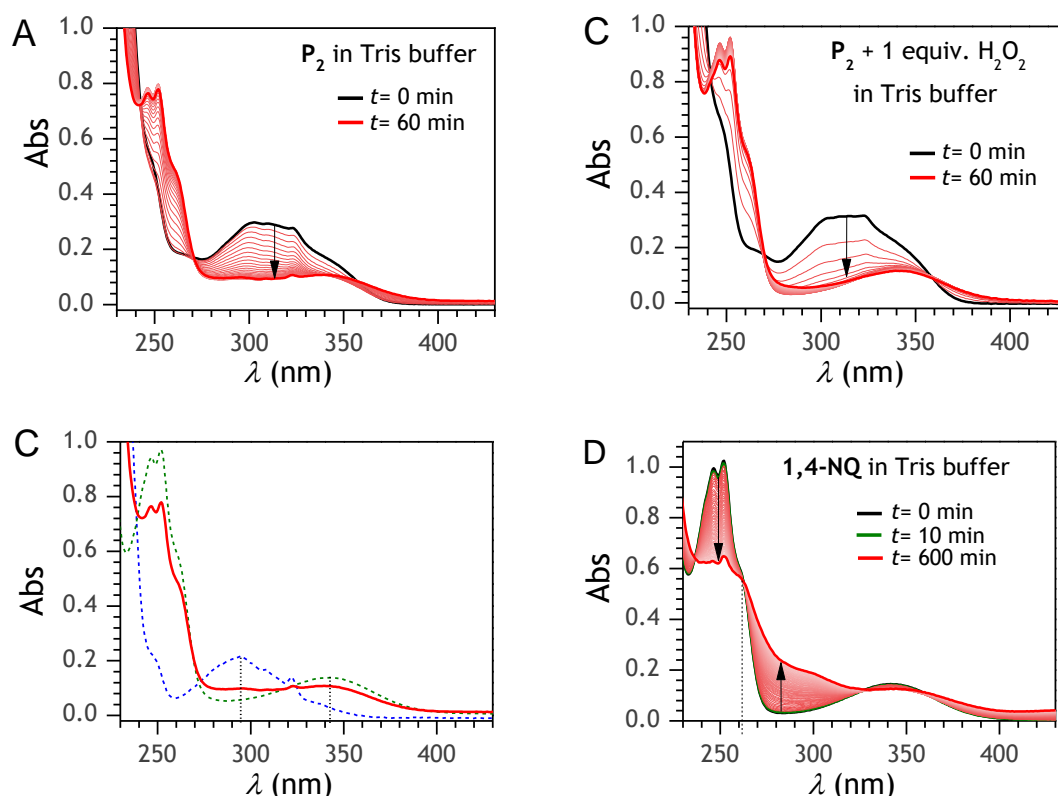


Figure S2. (A) UV-vis spectra of a freshly prepared solution of P_2 (50 μM) as a function of time in a 0.1 M Tris buffer at pH 8.5 (with 10 μM EDTA). The starting spectrum is highlighted in black, while the subsequent ones in red were recorded every 60 s over 60 min. (B) Same as in A but in the presence of 1 equiv. H_2O_2 . (C) The last spectrum in A recorded after 60 min (solid red line) is compared with the UV-vis spectra of a solution of 50 μM 1-naphthol (dashed blue line) and 50 μM 1,4-NQ (dashed green line) in the same Tris buffer. (D) Evolution of the UV-vis spectrum of a 50 μM solution of 1,4-NQ in a 0.1 M Tris buffer at pH 8.5. The spectra were recorded every 10 min. The vertical dashed line is positioned at the isobetic point at 262 nm.

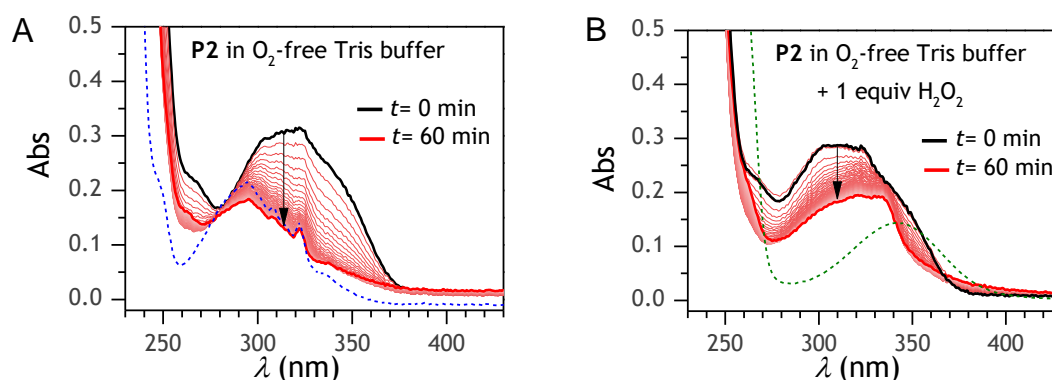


Figure S3. (A) UV-vis spectra of a freshly prepared solution of P_2 (50 μM) as a function of time in a O_2 -free buffer solution (*i.e.*, a 0.1 M Tris buffer at pH 8.5 thoroughly degassed with argon). The starting spectrum is highlighted in black, while the subsequent ones in red were recorded every 60 s over 1 hr. The blue dotted plot is the spectra obtained for a solution of 50 μM 1-naphthol in a non-degassed Tris buffer. (B) Same experience as in A but in the presence of 1 equiv. H_2O_2 . The starting spectrum is highlighted in black, while the subsequent ones in red were recorded every 10 s over 15 min. The green dotted plot is the spectra of a freshly prepared solution of 50 μM 1,4-NQ in a non-degassed Tris buffer.

4. HPLC analysis of the time course evolution of P_2 in a Tris buffer

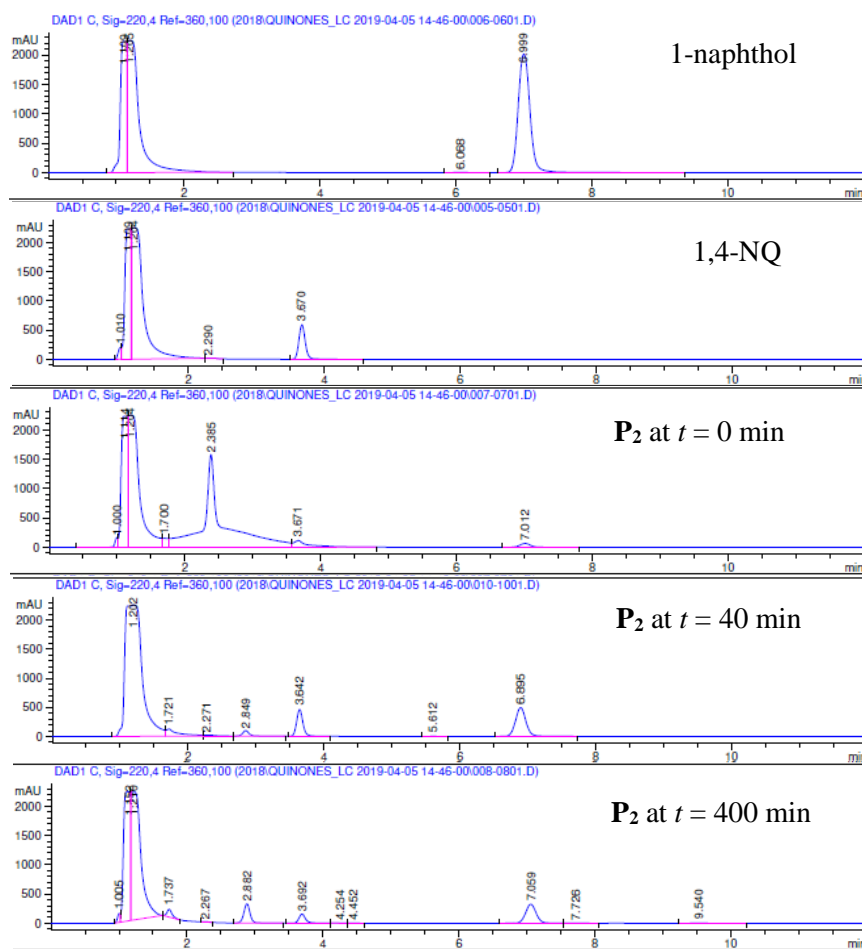


Figure S4. HPLC chromatograms recorded after injection of a 250 μ M solution of (from top to bottom) 1-naphthol, 1,4-NQ, and P_2 either freshly prepared ($t = 0$ min) or after being incubated for 40 min or 400 min. All solutions were prepared in a Tris-EDTA buffer at pH 8.5.

5. Kinetic analysis of the H₂O₂-mediated deprotection of P₂

The deprotection of P₂ by H₂O₂ can be basically described by the following set of reactions:

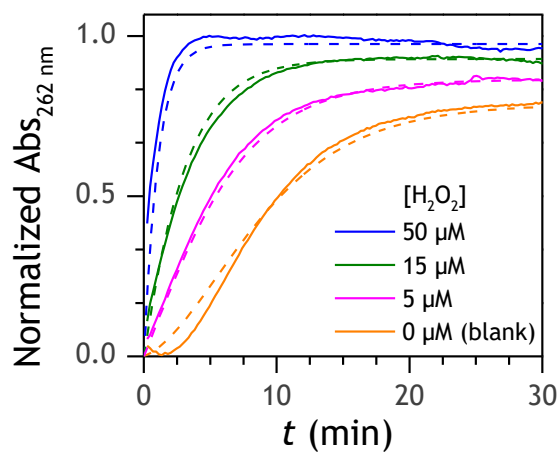
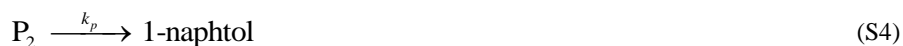


Figure S5. Normalized time-course absorbance changes at 262 nm for solutions of 50 μM P₂ mixed with different concentrations of H₂O₂ (ranging from 0 to 50 μM as indicated on the graph) in a 0.1 M Tris buffer at pH 8.5 (with 10 μM EDTA). Each plot is the average of triplicate experiments. The dashed curves correspond to the theoretical kinetic traces numerically calculated from the reaction scheme reported above (eqs. S1 to S4) and assuming that [O₂] remains constant during the whole process (*i.e.*, 0.25 mM at 1 atm.). The best fits of the simulated curves to the experimental plots were obtained using the following set of rate constants: $k_d = 300 \text{ M}^{-1} \text{ s}^{-1}$, $k_{ox} = 3300 \text{ M}^{-1} \text{ s}^{-1}$, $k_n = 1.2 \text{ M}^{-1} \text{ s}^{-1}$, and $k_p = 0.0004 \text{ s}^{-1}$.

6. UV-vis spectrophotometric characterization of P_3 either in the absence or presence of H_2O_2 .

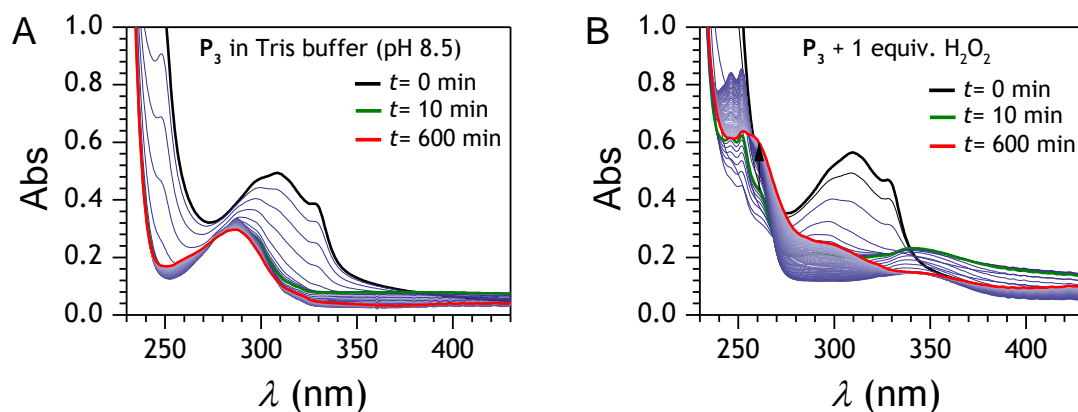


Figure S6. (A) UV-vis spectra of a freshly prepared diluted solution of P_3 (50 μ M) as a function of time in a 0.1 M Tris buffer at pH 8.5 (with 10 μ M EDTA). The starting spectrum is highlighted in black, while the subsequent ones in violet were recorded every 60 s during the first 10 min and then every 10 min over 10 hrs. The spectrum in green is after 10 min. (B) Same experience as in A but in the presence of 1 equiv. H_2O_2 .

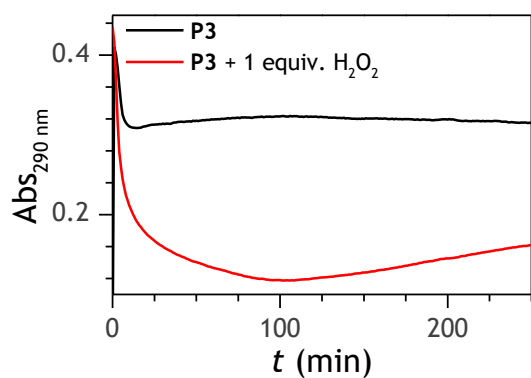


Figure S7. Kinetic traces at 290 nm (specific to the probe absorbance) recovered from the spectra in Figure S6.

7. Kinetic analysis of the H₂O₂-mediated deprotection of P₃.

The deprotection of P₃ by H₂O₂ can be basically described by the following set of reactions:

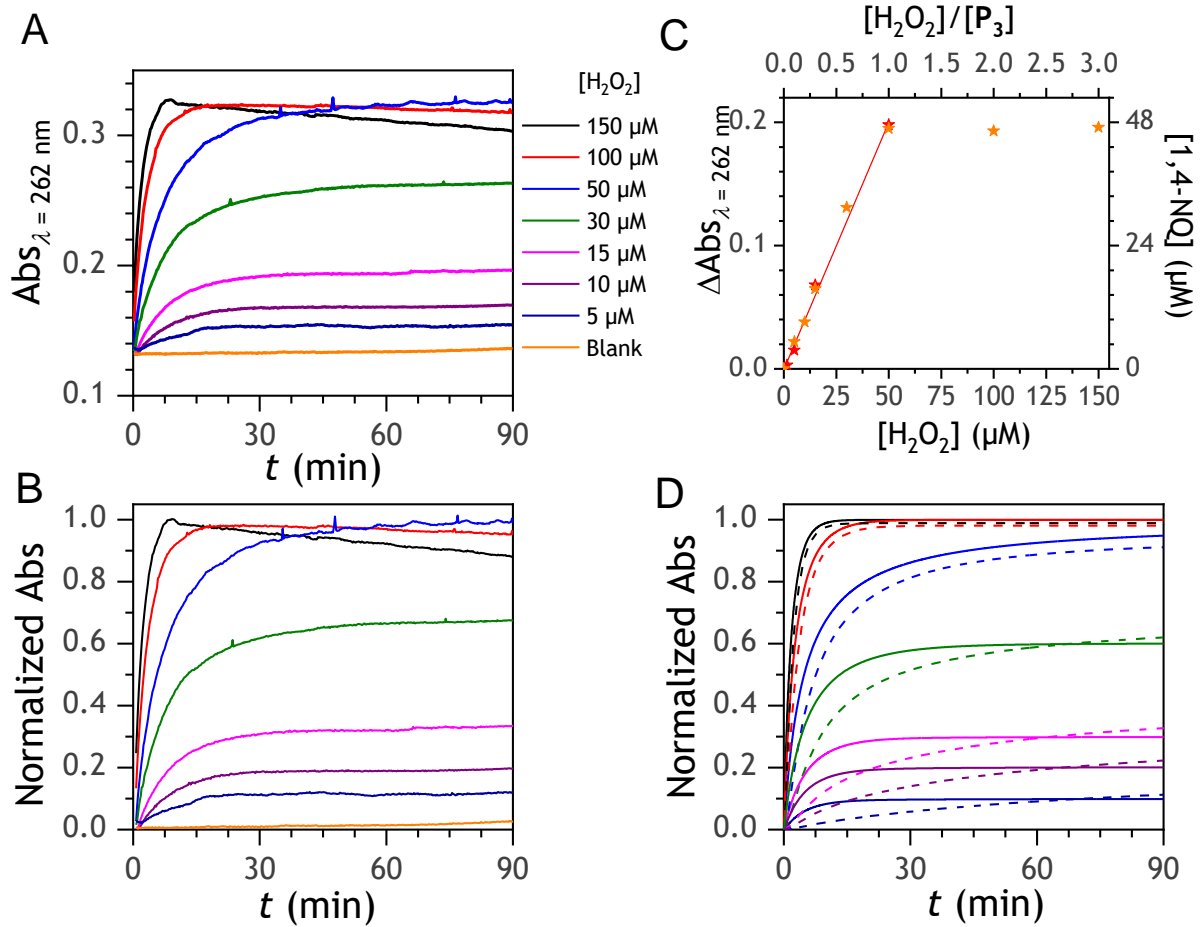
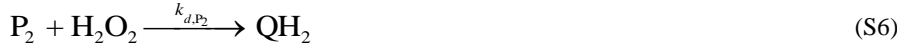


Figure S8. (A) Time-course absorbance changes at 262 nm for solutions of 50 μM P₃ mixed with different concentrations of H₂O₂ (ranging from 0 to 150 μM as indicated on the graph) in a 0.1 M Tris buffer at pH 8.5 (containing 10 μM EDTA). Each plot is the average of triplicate experiments. (Note that to avoid the interference of the initial absorbance change resulting from the hydrolysis of pinacol residues, H₂O₂ was added to the probe solutions after a delay of ~15 min to allow for complete probe hydrolysis into its diboric acid form). (B) Same than in A after absorbance normalization. (C) Maximal variation of absorbance (ΔAbs_{262 nm}) recorded at the end of the reaction as a function of H₂O₂ concentration. The straight line is the linear regression fit: $\Delta\text{Abs}_{262 \text{ nm}} = 0.00401 \times [\text{H}_2\text{O}_2] - 5 \times 10^{-4}$ ($r^2 = 0.995$). From the slope of the linear regression and the difference of extinction coefficients of probe and 1,4-NQ ($\Delta\epsilon = 7010 \text{ M}^{-1} \text{ cm}^{-1}$), the scale $\Delta\text{Abs}_{262 \text{ nm}}$ was converted in concentration of 1,4-NQ generated in microwells (see right axis). (D) Theoretical kinetic traces numerically simulated from the above reaction scheme (eqs. S5 to S9), assuming [O₂] constant and using the following set of rate constants: (dashed lines) $k_{d,P_3} = 35 \text{ M}^{-1} \text{ s}^{-1}$, $k_{d,P_2} = 300 \text{ M}^{-1} \text{ s}^{-1}$, $k_{ox} = 3300 \text{ M}^{-1} \text{ s}^{-1}$, $k_n = 1.2 \text{ M}^{-1} \cdot \text{s}^{-1}$, and $k_p = 0.0004 \text{ s}^{-1}$, or (solid lines) $k_{d,P_3} = 35 \text{ M}^{-1} \text{ s}^{-1}$, $k_{d,P_2} > 3000 \text{ M}^{-1} \text{ s}^{-1}$, $k_{ox} = 3300 \text{ M}^{-1} \text{ s}^{-1}$, $k_n = 1.2 \text{ M}^{-1} \cdot \text{s}^{-1}$, and $k_p = 0.0004 \text{ s}^{-1}$.

8. Autocatalytic reaction scheme involving P₃ and NADH/diaphorase and its numerical simulations

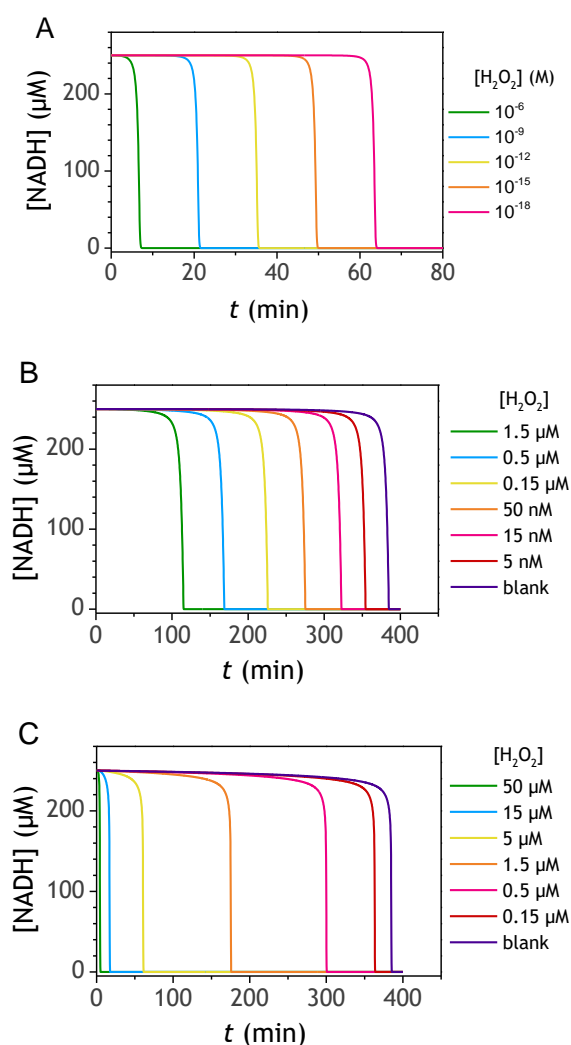


Figure S9. Theoretical kinetic traces at different H₂O₂ concentrations (see the caption on the graph) numerically calculated using: (A) the reaction scheme described by eqs. S10 to S16 and the rate constants gathered in the entry 1 of Table 1, (B) the reaction scheme reported in Scheme 3 and the rate constants gathered in the entry 2 of Table 1, (C) the reaction scheme reported in Scheme 3 and the rate constants gathered in the entry 4 of Table 1. In all simulations, the probe, enzyme, and substrate concentrations are the same as for the experiments (*i.e.* 50 μM, 10 nM, and 250 μM, respectively).

9. Justification of the rate constants used in the autoxidation mechanism of 1,4-NQ

The different rate constants characterizing the reactions 0 to 5 of the free-radical chain autoxidation mechanism of 1,4-NQ (see the main text of the manuscript) were obtained as follow. The value of $k_{dis,4}$ at pH 8.5 (*i.e.*, $2 \times 10^4 \text{ M}^{-1}\cdot\text{s}^{-1}$) was recovered from the literature.^{S4} The equilibrium constant of the outer-sphere one-electron transfer reaction 2 (*i.e.*, $K_2 = k_2/k_{-2}$) is, according to the Marcus theory, governed by the position of the one-electron reduction potential of $Q/Q^{\bullet-}$ ($E_{Q/Q^{\bullet-}}^{0'} = -0.140 \text{ V vs. NHE}$ at physiological pHs^{S5,S6,S7}) relative to that of $O_2/O_2^{\bullet-}$ ($E_{O_2/O_2^{\bullet-}}^{0'} = -0.180 \text{ V vs. NHE}$ ^{S8}), and so by the following Nernst equation:

$$\Delta E_2 = E_{O_2/O_2^{\bullet-}}^{0'} - E_{Q/Q^{\bullet-}}^{0'} = RT/F \ln K_2$$

The resulting slightly negative driving force (*i.e.*, $\Delta E_2 = -40 \text{ mV}$) means that the one-electron oxidation of 1,4-NQ $^{\bullet-}$ by O_2 , although kinetically fast, is thermodynamically slightly unfavorable (*i.e.*, $K_2 = 0.2$ at 20°C). Considering the backward rate constant previously determined by pulse radiolysis for reaction 2,^{S9} *i.e.* $k_{-2} = 2 \times 10^8 \text{ M}^{-1}\cdot\text{s}^{-1}$, a forward rate constant $k_2 = 4.4 \times 10^7 \text{ M}^{-1}\cdot\text{s}^{-1}$ can be calculated. These values are in good agreement with the rate constants of $k_2 = 3.7 \times 10^7 \text{ M}^{-1}\cdot\text{s}^{-1}$ and $k_{-2} = 1.8 \times 10^8 \text{ M}^{-1}\cdot\text{s}^{-1}$ reported by Loeff et al.^{S10} The pH-dependant equilibrium constant K_I , characterizing the equilibrated comproportionation/disproportionation reaction of 1,4-NQ, was recovered from the literature with a value of 6.7×10^{-21} at pH = 0.^{S11} Considering the acidity constants of 1,4-NQH₂ ($pK_{a,1} = 9.48$ and $pK_{a,2} = 11.02$ ^{S12}), the value of K_I at pH 8.5 can be estimated to be $k_{co,1}/k_{dis,-1} = 7 \times 10^{-4}$. For a wide range of semiquinone radicals, the disproportionation rate constants were reported to be fast and close to the diffusion limit (ranging from $k_{dis,-1} = 3 \times 10^7 \text{ M}^{-1}\cdot\text{s}^{-1}$ to $2 \times 10^8 \text{ M}^{-1}\cdot\text{s}^{-1}$ at physiological pHs^{S9,S13,S14,S15,S16}). As a result, assuming an average $k_{dis,-1}$ value of $10^8 \text{ M}^{-1}\cdot\text{s}^{-1}$, a comproportionation rate constant of $k_{co,1} = 6.6 \times 10^4 \text{ M}^{-1}\cdot\text{s}^{-1}$ was assumed for the 1,4-NQ at pH 8.5 (it is important to note that on account of the double pH dependency of K_I , the value of $k_{co,1}$ changes significantly with the pH). Another possibility to access the value of $k_{co,1}$ is from the knowledge of the one-electron reduction potentials of the redox couples $Q/Q^{\bullet-}$ (-0.140 V vs. NHE) and $Q^{\bullet-}/Q^{2-}$ (-0.131 V vs. NHE ^{S17}). Indeed, using the following Nernst equation:

$$\Delta E_1 = E_{Q/Q^{\bullet-}}^{0'} - E_{Q^{\bullet-}/Q^{2-}}^{0'} = RT/F \ln K_1$$

we can calculate $K_I = 0.7$ at pH = 0 (and 20°C) and therefore $K_I = 2.2 \times 10^{-4}$ at pH 8.5, which is finally in good agreement with the above value of K_I at the same pH. The information on k_3 in the literature is scarce and contradictory. It is expected to be in the range of 10^4 - $10^5 \text{ M}^{-1}\cdot\text{s}^{-1}$,^{S13,S17} sufficiently slow for being unable to compete efficiently under aerobic conditions with the fast reaction of semiquinones with dioxygen (reaction 2). However, as we will see this reaction can be critical in controlling the redox cycling and thus in controlling the autocatalytic process. We therefore considered this reaction with care in our simulations using, at first, the same k_3 value reported by Waite and coll. (*i.e.*, $8 \times 10^4 \text{ M}^{-1}\cdot\text{s}^{-1}$).^{S17} As we will see, this value was thereafter slightly adjusted to better fit our results. It is also worth to note that k_3 is expected to increase when the reduction potential $E_{Q^{\bullet-}/QH_2}^{0'}$ decreases and also, similarly as to $k_{co,1}$, to vary significantly with the pH. A more problematic rate constant to define precisely is k_0 because, like k_3 , it is difficult to determine independently.^{S17} Moreover, changing its value has a similar effect to that of changing k_3 , both contributing to the consumption of QH₂. For our simulations, we have thus considered k_0 as always sufficiently small so that its influence on the simulations is negligible. A value of $0.001 \text{ M}^{-1}\cdot\text{s}^{-1}$ was thus systematically used. Concerning the last rate constant characterizing the cross-dismutation reaction 5 (also the chain-termination reaction), it is generally assumed to be very fast because thermodynamically highly favorable considering the high formal reduction potential of the couple $O_2^{\bullet-}/H_2O_2$ ^{S18} relative to that of $Q/Q^{\bullet-}$, even at pH 8.5. A rate constant value of $k_5 = 2 \times 10^9 \text{ M}^{-1}\cdot\text{s}^{-1}$, close to the diffusion limit was thus assumed.^{S17}

10. Determination of the enzyme rate constants k_3 and k_{red} from redox cycling experiments with 1,4-NQ and their analysis by numerical simulations

From the zero-order kinetics slopes obtained in redox cycling experiments (a set of kinetic curves is shown in graph A of Figure S10) the graph B of Figure S10 was drawn. The latter indicates two kinetic regimes as a function of 1,4-NQ concentration, with a transition between a slow and fast regime at around 5 μM . This behavior suggests the passage from a kinetic control by the 1,4-NQH₂ autoxidation to a kinetic control by the enzymatic reduction in the redox cycle (see Figure S11). However, on account of the intricate mechanism governing the autoxidation of 1,4-NQ, it is not trivial to establish clearly the key parameters governing this transition, and this is the reason why we attempted to do that through simulation of the redox cycling mechanism presented in Figure S11. For such a purpose, we started with the same rate constants that were used to simulate the autocatalytic responses in Figure 4 and then we progressively changed k_3 and k_{red} in different proportions to assess their respective influence on the redox cycling kinetics. The simulated plots (overlaid to the experimental data in graph B of Figure S10) show an effective transition between two kinetic regimes. Interestingly, it moves from the left to the right position when k_{red} is raised, while it shifts up and down essentially through the ratio k_3/k_{red} (which in fact measures the competition between the rate of disappearance of 1,4-NQH₂ by autoxidation and the rate of regeneration of this same 1,4-NQH₂ by the enzymatic reduction). Consequently, one should expect to recover the absolute values of k_3 and k_{red} from the best fits of simulated plots to the experimental data. This is what it has been done in graph B of Figure S10, but with the difficulty of reproducing the positioning of the transition observed in the experimental graph, as well as the rates of NADH consumption at the highest concentrations of 1,4-NQ. Nevertheless, this allowed us to estimate with a reasonably good degree of confidence the values of k_3 and k_{red} , the former being in the range $(5 - 8) \times 10^4 \text{ M}^{-1}\cdot\text{s}^{-1}$ and the latter closer to $(1.5 - 0.8) \times 10^8 \text{ M}^{-1}\cdot\text{s}^{-1}$ rather than $1.5 \times 10^9 \text{ M}^{-1}\cdot\text{s}^{-1}$.

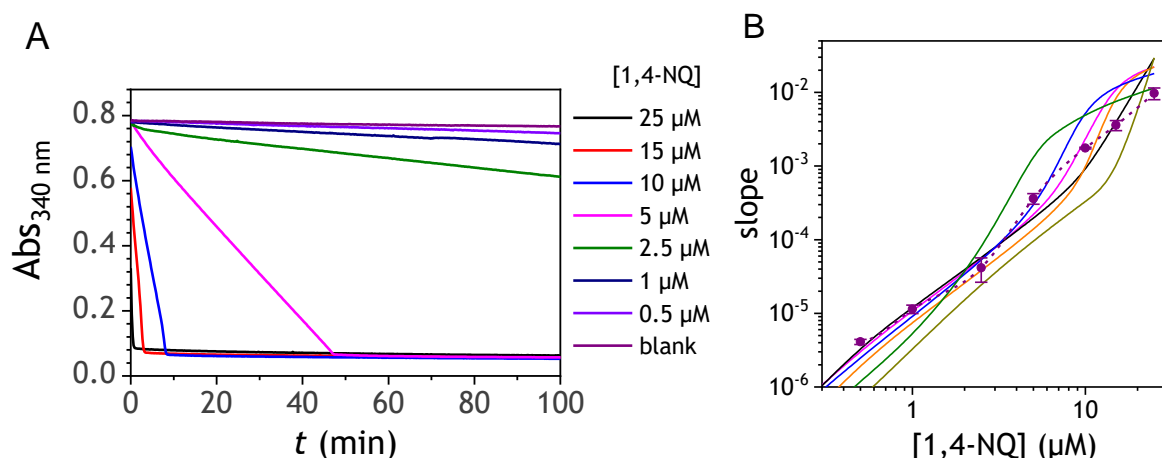
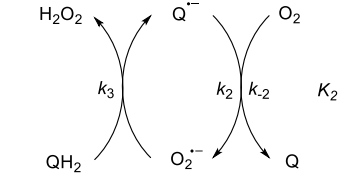


Figure S10. (A) Absorbance traces (measuring the NADH consumption at 340 nm) recorded during redox cycling experiments. The reactions were initiated by mixing different concentrations of 1,4-NQ (see caption on the graph) to solutions containing 10 nM DI and 250 μM NADH in a 0.1 M Tris buffer (pH 8.5). The slopes of these zero-order kinetics were used to draw the graphs in B. (B) The purple dots are the apparent rate constants of the redox cycling as a function of the 1,4-NQ concentration (the purple dashed line is to help the visualization). The solid lines were obtained from the simulation of the redox cycling reaction scheme depicted in Figure S11, using the same rate constants as those already reported for the autoxidation reactions of 1,4-NQH₂ (*i.e.*, $k_0 = 0.001 \text{ M}^{-1}\cdot\text{s}^{-1}$, $k_{co,1} = 66000 \text{ M}^{-1}\cdot\text{s}^{-1}$, $k_{dis,-1} = 10^8 \text{ M}^{-1}\cdot\text{s}^{-1}$, $k_2 = 4.4 \times 10^7 \text{ M}^{-1}\cdot\text{s}^{-1}$, $k_2 = 2 \times 10^8 \text{ M}^{-1}\cdot\text{s}^{-1}$, $k_4 = 2 \times 10^4 \text{ M}^{-1}\cdot\text{s}^{-1}$, $k_5 = 2 \times 10^9 \text{ M}^{-1}\cdot\text{s}^{-1}$) and enzyme reactions (*i.e.*, $K_M = 60 \mu\text{M}$, $k_c = 1200 \text{ s}^{-1}$) except for the values of k_3 and k_{red} which were varied as follows: (dark yellow) $k_3 = 8 \times 10^4 \text{ M}^{-1}\cdot\text{s}^{-1}$, $k_{red} = 1.5 \times 10^9 \text{ M}^{-1}\cdot\text{s}^{-1}$, (black) $k_3 = 8 \times 10^4 \text{ M}^{-1}\cdot\text{s}^{-1}$, $k_{red} = 1.5 \times 10^8 \text{ M}^{-1}\cdot\text{s}^{-1}$, (orange) $k_3 = 5 \times 10^4 \text{ M}^{-1}\cdot\text{s}^{-1}$, $k_{red} = 10^8 \text{ M}^{-1}\cdot\text{s}^{-1}$, (magenta) $k_3 = 2 \times 10^4 \text{ M}^{-1}\cdot\text{s}^{-1}$, $k_{red} = 8 \times 10^8 \text{ M}^{-1}\cdot\text{s}^{-1}$, (blue) $k_3 = 5 \times 10^4 \text{ M}^{-1}\cdot\text{s}^{-1}$, $k_{red} = 5 \times 10^7 \text{ M}^{-1}\cdot\text{s}^{-1}$, and (green) $k_3 = 2 \times 10^4 \text{ M}^{-1}\cdot\text{s}^{-1}$, $k_{red} = 2 \times 10^7 \text{ M}^{-1}\cdot\text{s}^{-1}$.



15

11. Numerical simulation of the autocatalysis with P_2

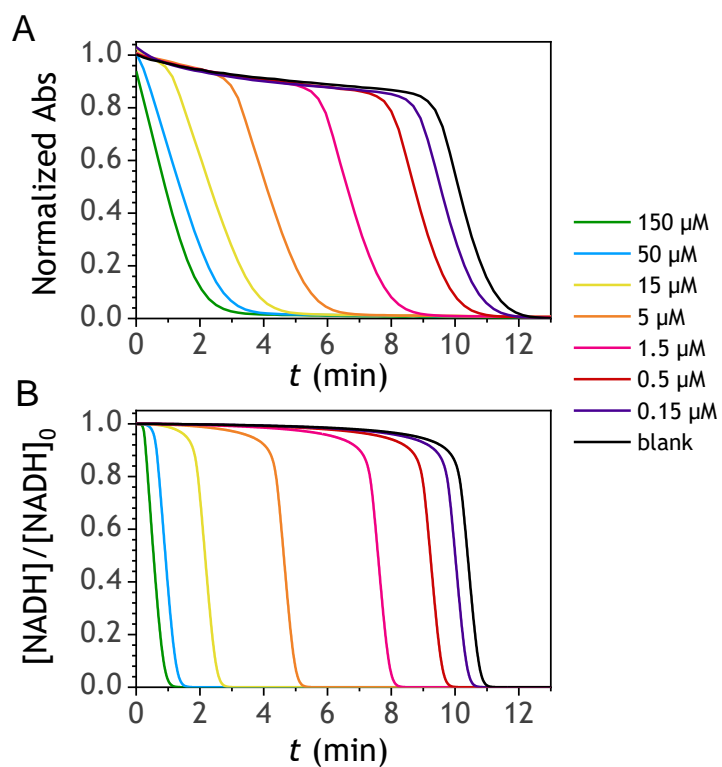


Figure S12. Comparison of (A) the experimental kinetic plots obtained with P_2 (same data than in Figure 1A but normalized here to the maximal absorbance amplitude) with (B) those numerically simulated from the model reported in Scheme 3 and using the rate constants in entry 6 of Table 1.

12. Influence of the buffer nature and pH on the autocatalytic reaction with P_3

12.1. Tris buffer ($pK_a = 8.1$)

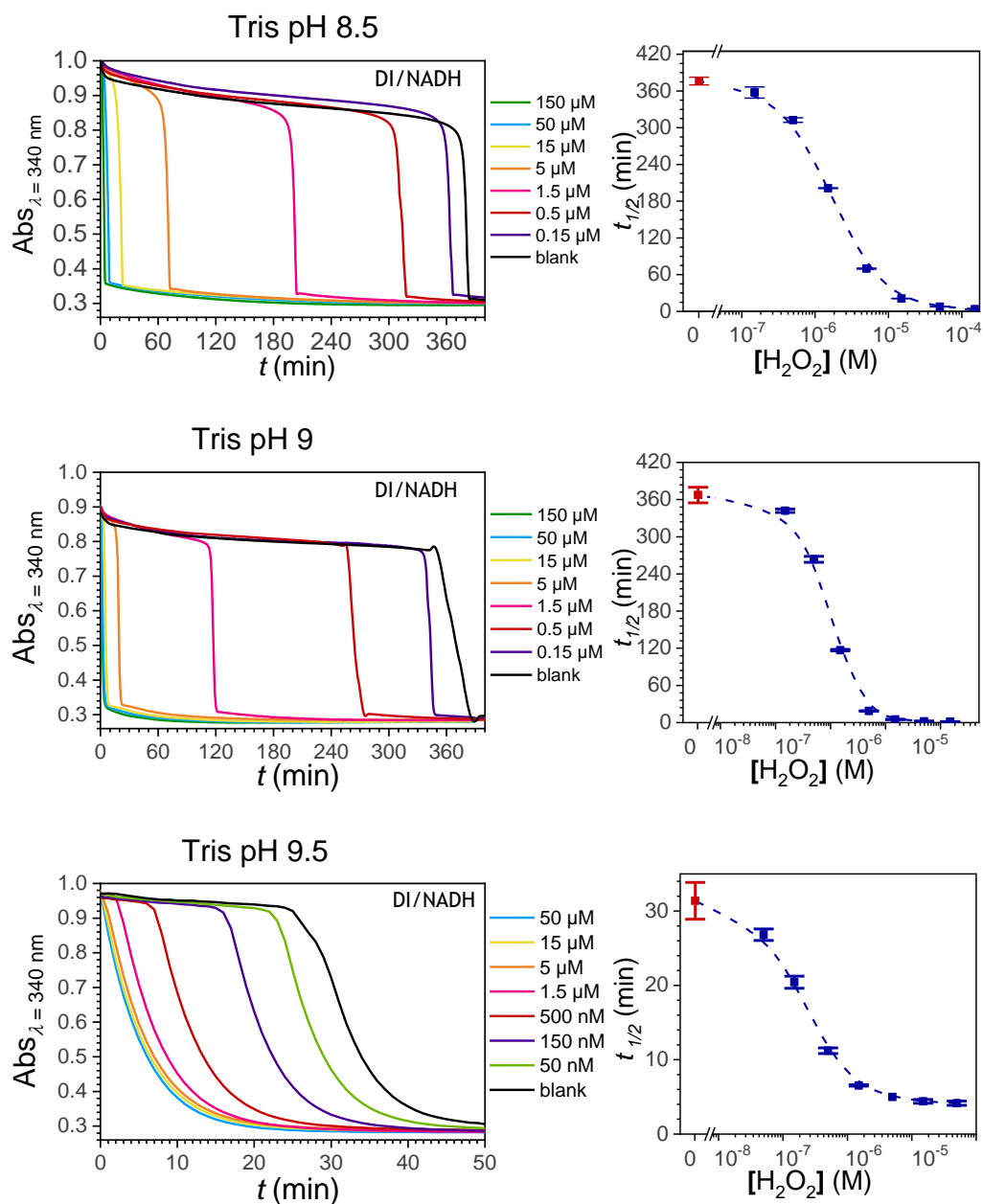


Figure S13. (Left) UV-vis kinetic traces (average of triplicates) monitored at 340 nm immediately after the injection of different concentrations of H_2O_2 (as indicated in the captions) to solutions containing 50 μM P_3 , 10 nM DI and 250 μM NADH in 0.1 M Tris buffers (containing 10 μM EDTA) at different pHs as indicated on the graphs. (Right) Corresponding semi-logarithmic H_2O_2 calibration plots. Errors bars are standard deviations from triplicates.

12.2. *Bicine buffer* ($pK_a = 8.3$)

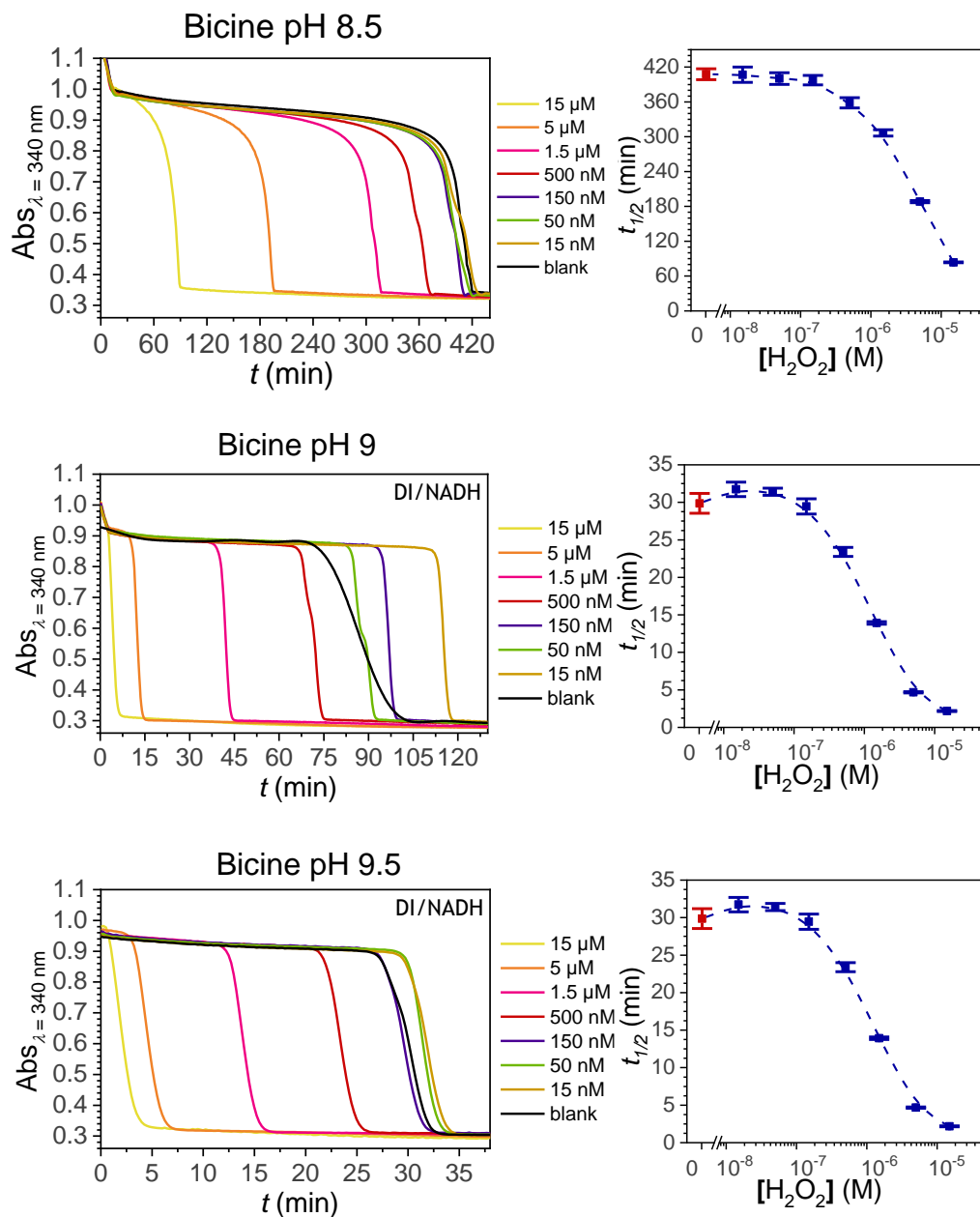


Figure S14. (Left) UV-vis kinetic traces (average of triplicates) monitored at 340 nm immediately after the injection of different concentrations of H_2O_2 (as indicated in the captions) to solutions containing 50 μM P_3 , 10 nM DI and 250 μM NADH in 0.1 M Bicine buffers (containing 10 μM EDTA) at different pHs as indicated on the graphs. (Right) Corresponding semi-logarithmic H_2O_2 calibration plots. Errors bars are standard deviations from triplicates.

12.3. CAPSO buffer ($pK_a = 9.6$)

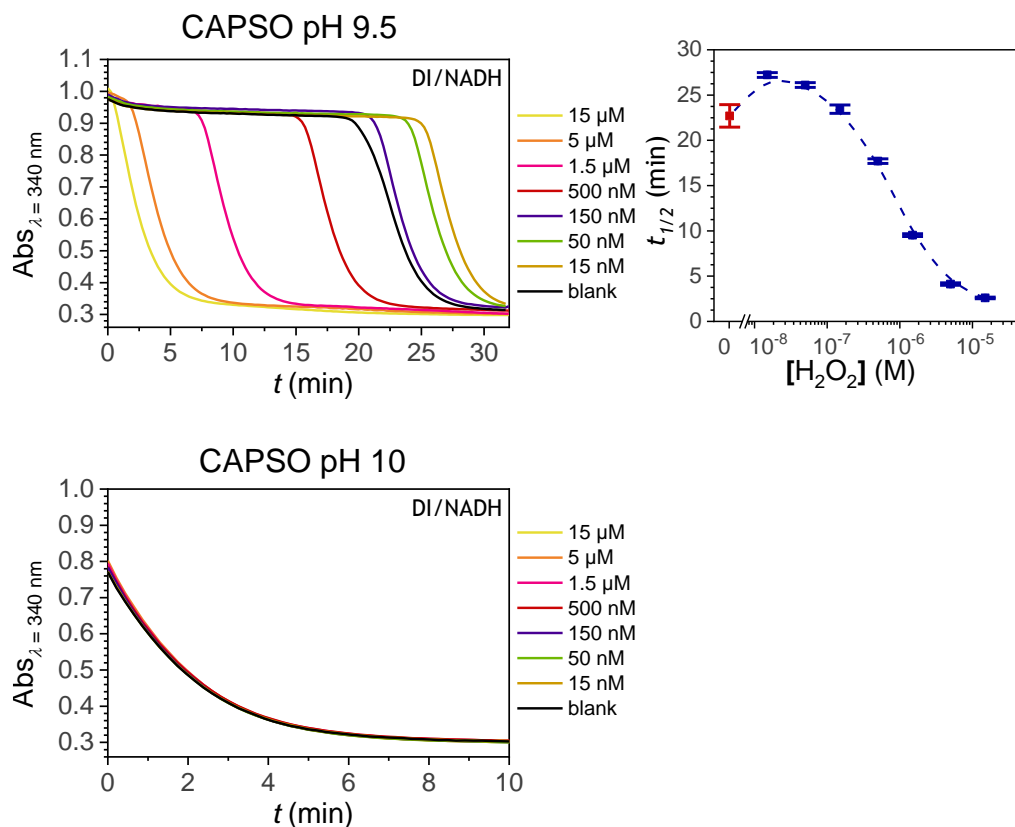


Figure S15. (Left) UV-vis kinetic traces (average of triplicates) monitored at 340 nm immediately after the injection of different concentrations of H_2O_2 (as indicated in the captions) to solutions containing 50 μM P_3 , 10 nM DI and 250 μM NADH in 0.1 M CAPSO buffers (containing 10 μM EDTA) at two different pHs as indicated on the graphs. (Right) Corresponding semi-logarithmic H_2O_2 calibration plots. Errors bars are standard deviations from triplicates.

12.4. CHES buffer ($pK_a = 9.3$)

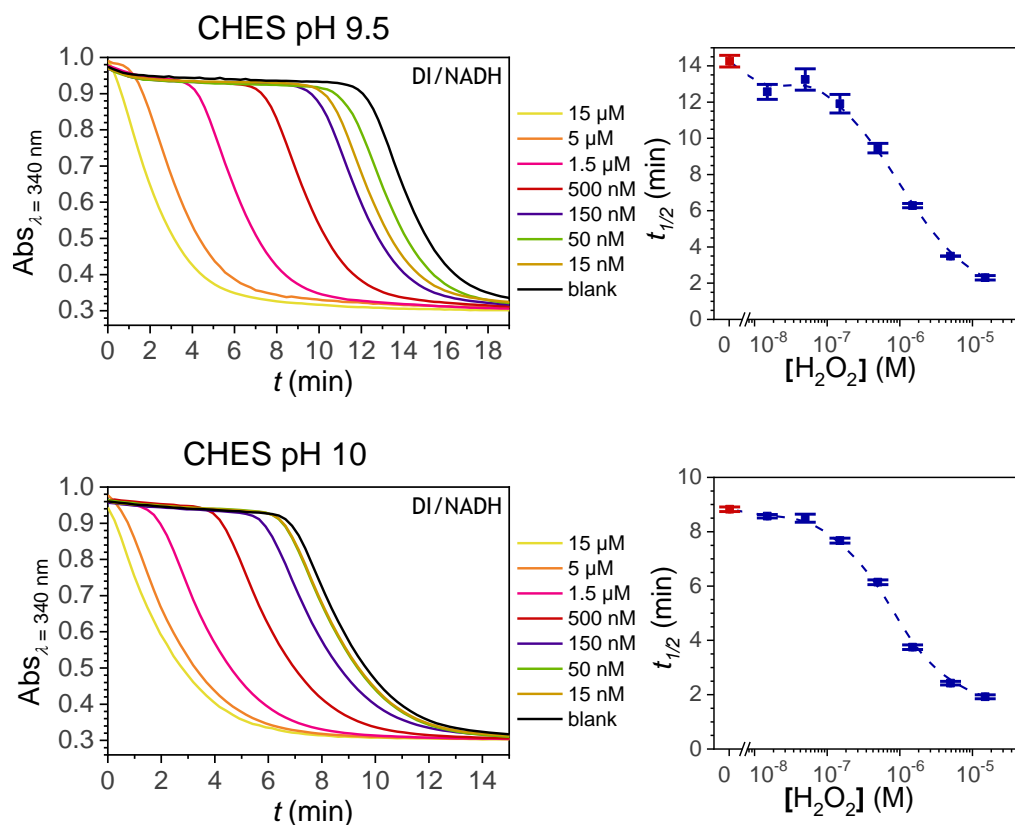


Figure S16. (Left) UV-vis kinetic traces (average of triplicates) monitored at 340 nm immediately after the injection of different concentrations of H_2O_2 (as indicated in the captions) to solutions containing 50 μM P_3 , 10 nM DI and 250 μM NADH in 0.1 M CHES buffers (containing 10 μM EDTA) at two different pHs as indicated on the graphs. (Right) Corresponding semi-logarithmic H_2O_2 calibration plots. Errors bars are standard deviations from triplicates.

12.5. Borate buffer (pKa = 9.3)

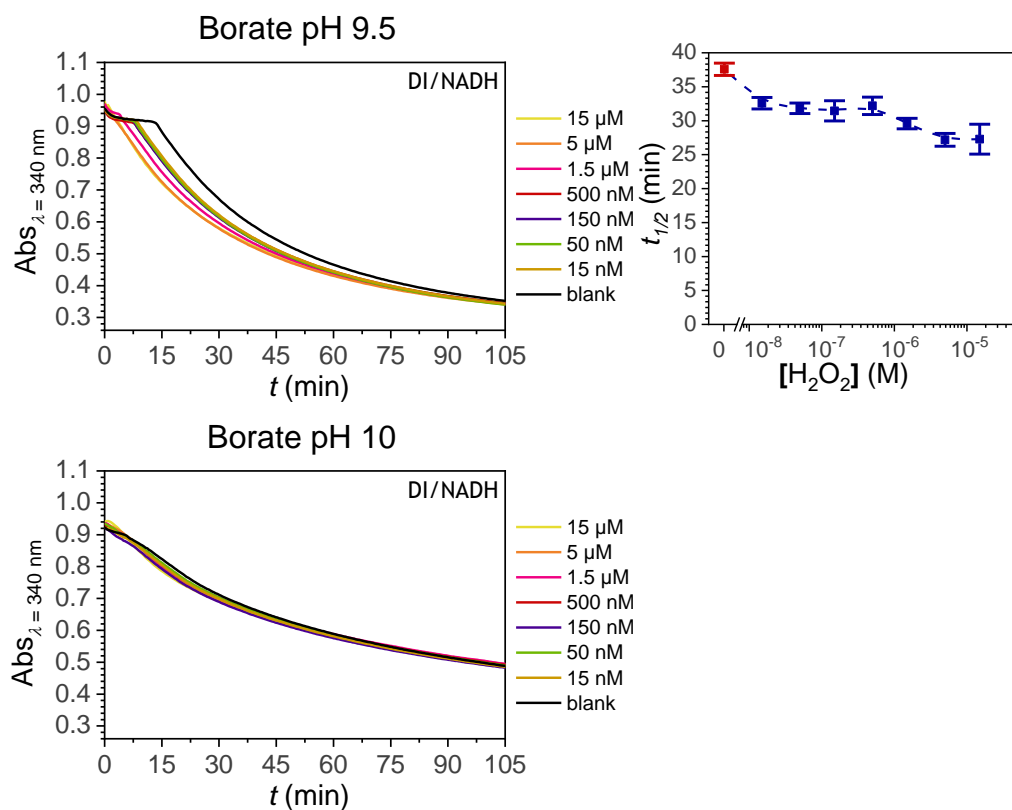


Figure S17. (Left) UV-vis kinetic traces (average of triplicates) monitored at 340 nm immediately after the injection of different concentrations of H₂O₂ (as indicated in the captions) to solutions containing 50 μM P₃, 10 nM DI and 250 μM NADH in 0.1 M Borate buffers (containing 10 μM EDTA) at two different pHs as indicated on the graphs. (Right) Corresponding semi-logarithmic H₂O₂ calibration plots. Errors bars are standard deviations from triplicates.

12.6. Glycine buffer ($pK_a = 9.6$)

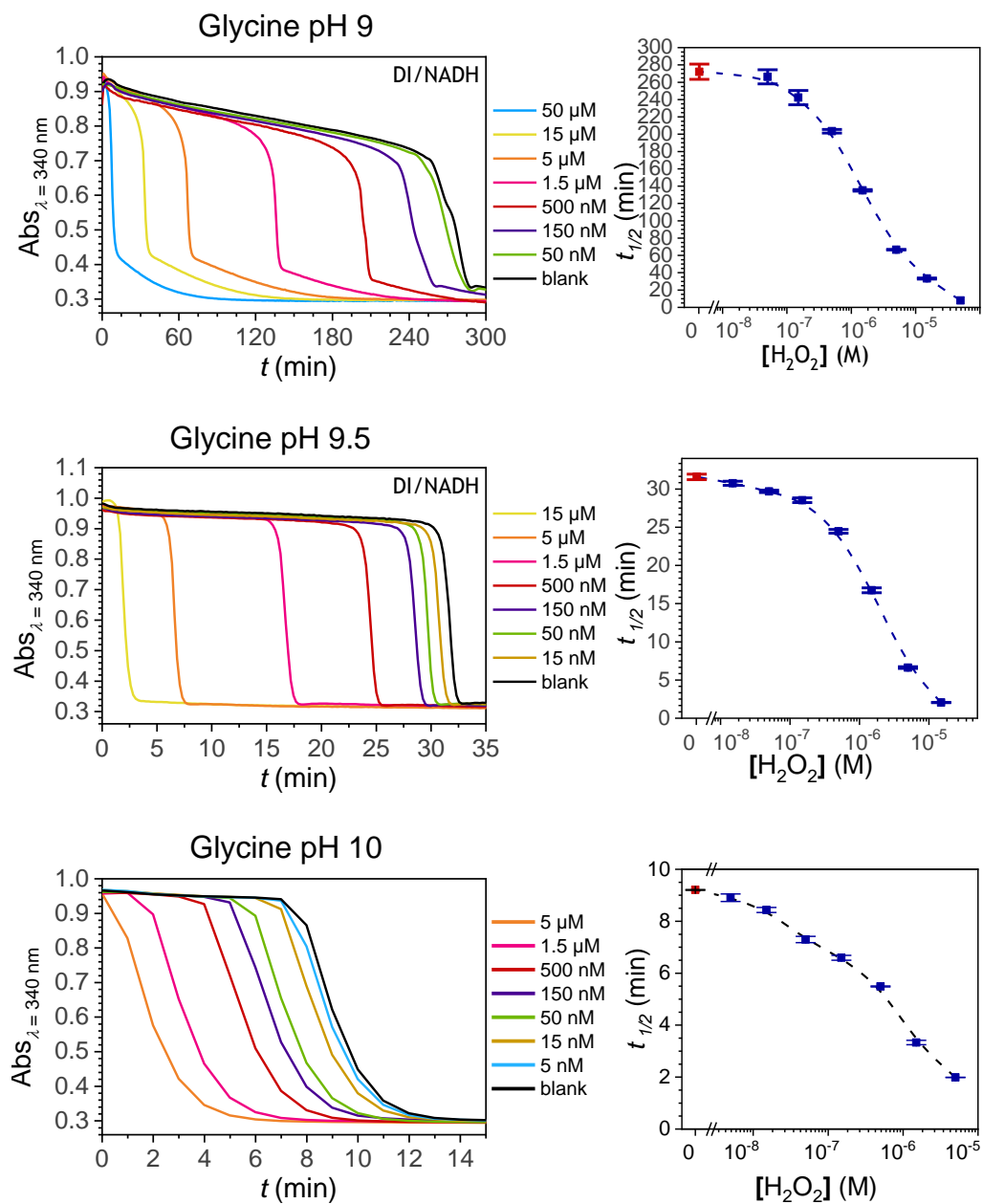


Figure S18. (Left) UV-vis kinetic traces (average of triplicates) monitored at 340 nm immediately after the injection of different concentrations of H_2O_2 (as indicated in the captions) to solutions containing 50 μM P_3 , 10 nM DI and 250 μM NADH in 0.1 M glycine buffers (containing 10 μM EDTA) at different pHs as indicated on the graphs. (Right) Corresponding semi-logarithmic H_2O_2 calibration plots. Errors bars are standard deviations from triplicates.

12.7. Carbonate buffer ($pK_a = 10.3$)

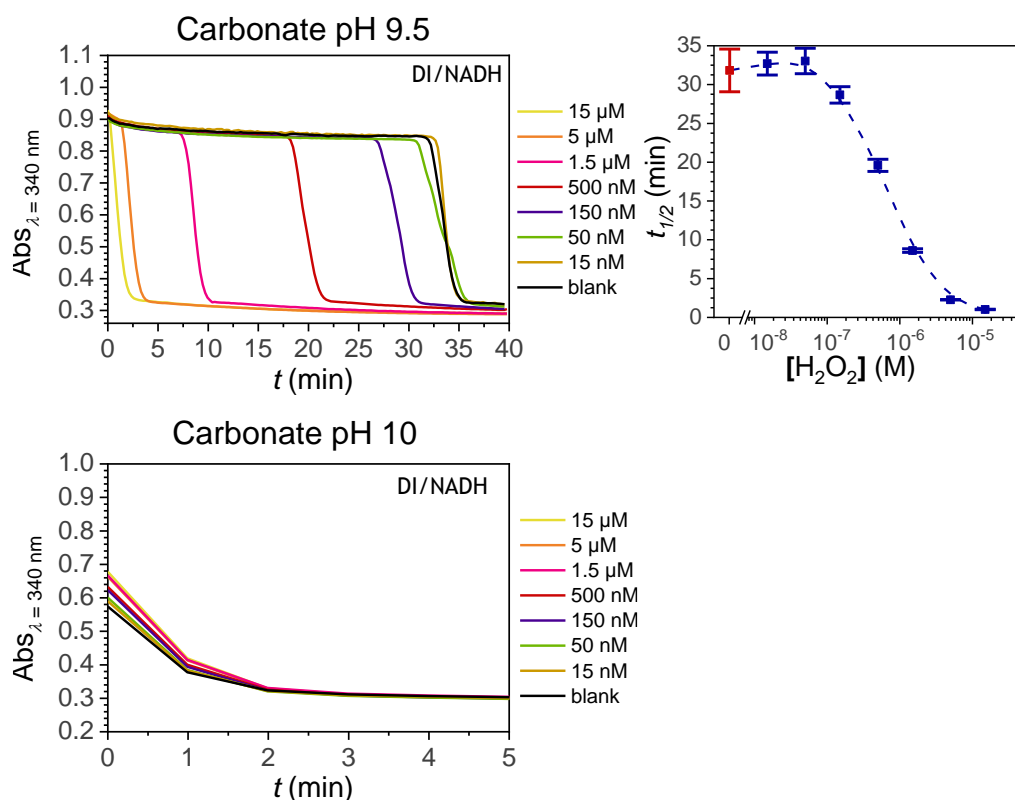


Figure S19. (Left) UV-vis kinetic traces (average of triplicates) monitored at 340 nm immediately after the injection of different concentrations of H_2O_2 (as indicated in the captions) to solutions containing 50 μM P_3 , 10 nM DI and 250 μM NADH in 0.1 M sodium carbonate buffers (containing 10 μM EDTA) at two different pHs as indicated on the graphs. (Right) Corresponding semi-logarithmic H_2O_2 calibration plots. Errors bars are standard deviations from triplicates.

12.8. CAPS buffer ($pK_a = 10.4$)

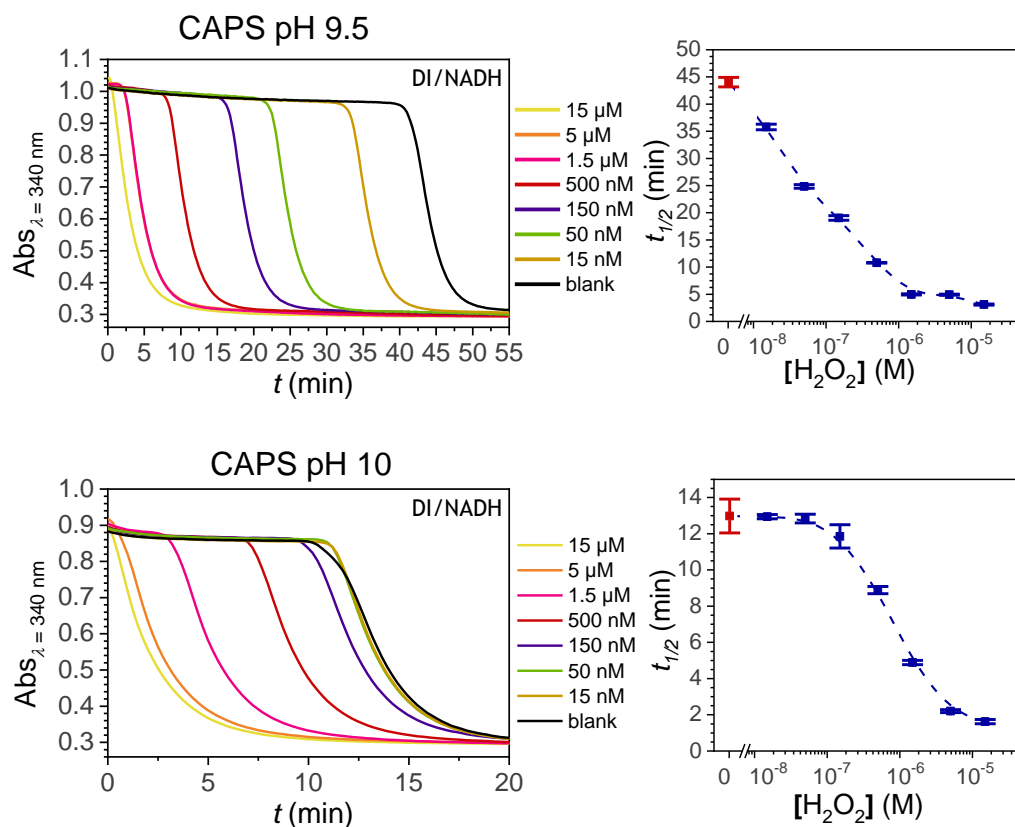


Figure S20. (Left) UV-vis kinetic traces (average of triplicates) monitored at 340 nm immediately after the injection of different concentrations of H_2O_2 (as indicated in the captions) to solutions containing 50 μM P_3 , 10 nM DI and 250 μM NADH in 0.1 M CAPS buffers (containing 10 μM EDTA) at two different pHs as indicated on the graphs. (Right) Corresponding semi-logarithmic H_2O_2 calibration plots. Errors bars are standard deviations from triplicates.

13. Screening of naphthoquinones for their redox cycling properties.

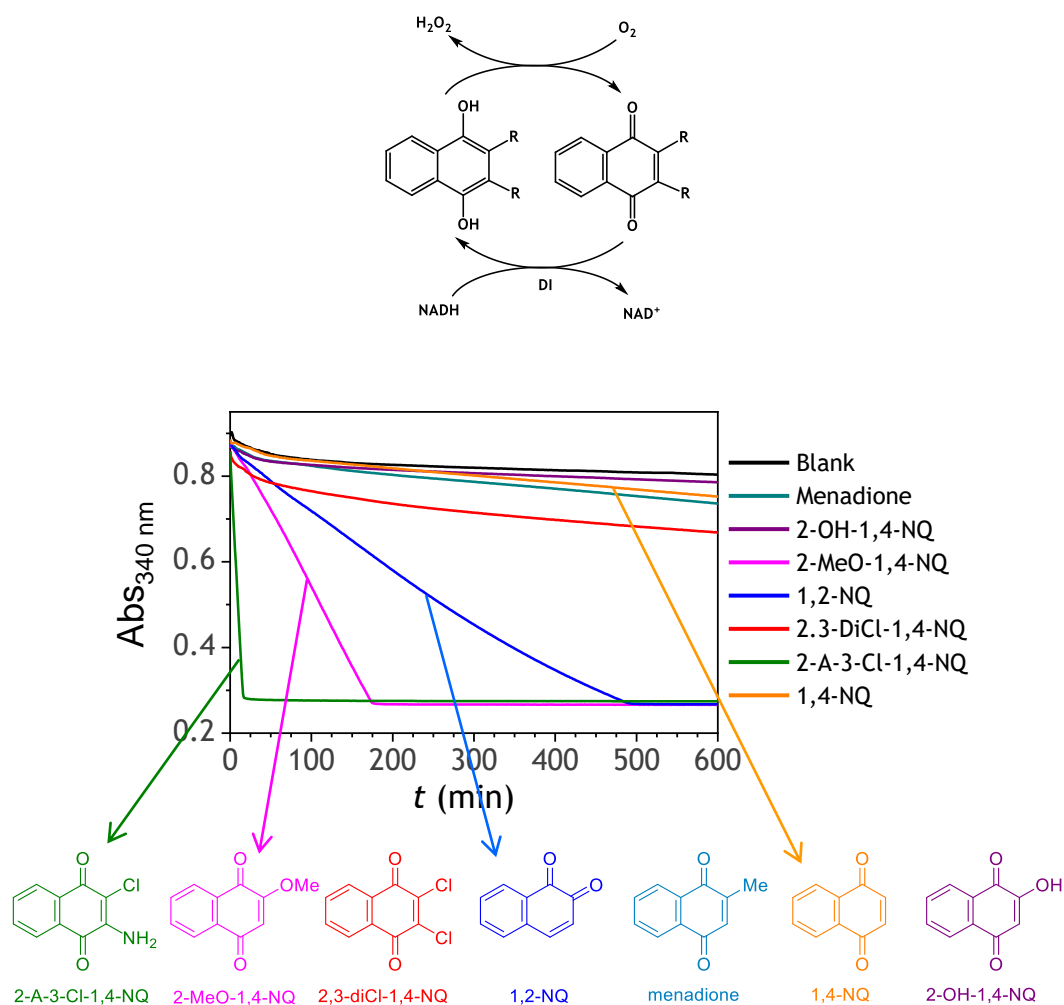


Figure S21. Screening of the redox cycling properties of a set of different naphthoquinones (the molecular structures of the selected naphthoquinones are shown above). The redox cycling kinetics shown on graph were obtained by monitoring at 340 nm the consumption of NADH (250 μ M) in the presence of DI (10 nM) and a catalytic amount (1 μ M) of one of the selected naphthoquinone (see the legend on the graph) in a Tris-EDTA buffer (pH 8.5).

14. UV-vis spectrophotometric characterization of P_4 (either in the absence or presence of H_2O_2) and 2-MeO-NQ.

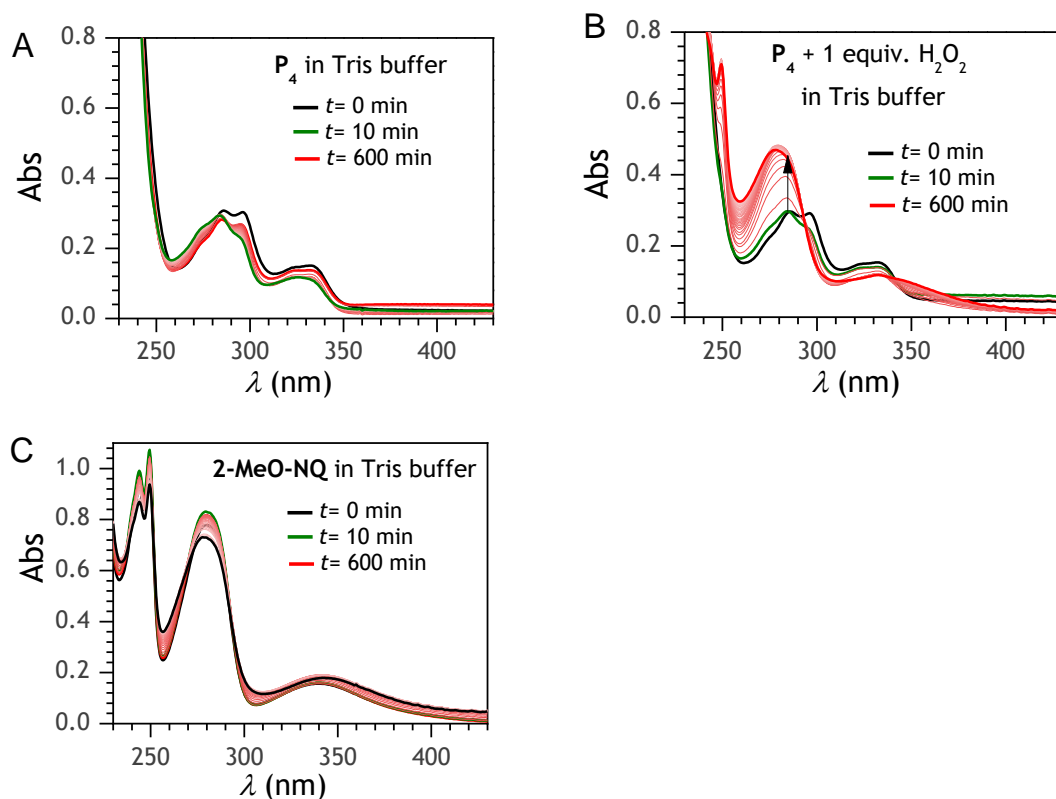


Figure S22. (A) UV-vis spectra of a freshly prepared dilute solution of P_4 (50 μ M) as a function of time in a 0.1 M Tris buffer at pH 8.5 (with 10 μ M EDTA). The starting spectrum is highlighted in black, the second spectrum in green was recorded after 10 minutes, and all subsequent spectra in red were recorded every 20 min over 10 hrs. (B) Same experience as in A but in the presence of 1 equiv. H_2O_2 . The arrow is positioned at 285 nm. (C) Evolution of the UV-vis spectrum of a 50 μ M solution of 2-MeO-NQ in a 0.1 M Tris buffer at pH 8.5. The spectra were recorded every 10 min. The vertical dashed line is positioned at the isobestic point at 262 nm.

15. Indirect detection of glucose oxidase (GOD)

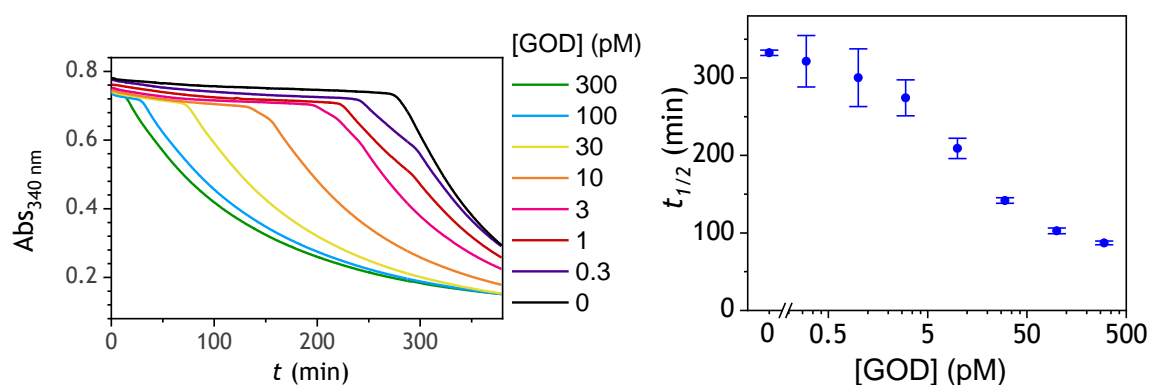


Figure S23. (A) UV-vis kinetic traces monitored at 340 nm immediately after the injection of different concentrations of GOD (as indicated in the caption on the graph) to solutions containing 50 μ M P_3 , 0.1 nM DI and 250 μ M NADH. All experiments were conducted in air-saturated Tris-EDTA buffers (0.1 M, pH 8.5). Each curve is the average of triplicate experiments. (B) Semi-logarithmic calibration curves obtained from the plot of $t_{1/2}$ as a function of GOD concentration.

16. References

- (S1) S. Hoops, S. Sahle, R. Gauges, C. Lee, J. Pahle, N. Simus, M. Singhal, L. Xu, P. Mendes, U. Kummer, COPASI - a Complex PATHway Simulator, *Bioinformatics*, **2006**, 22, 3067–74.
- (S2) R. Luebke, Y. Belmabkhout, Ł. J. Weseliński, A. J. Cairns, M. Alkordi, G. Norton, Ł. Wojtas, K. Adila, M. Eddaoudi, *Chem. Sci.*, **2015**, 6, 4095–102.
- (S3) M. W. A. MacLean, T. K. Wood, G. Wu, R. P. Lemieux, C. M. Crudden, *Chem. Mater.*, **2014**, 26, 5852–5859.
- (S4) B. H. J. Bielski, R. L. Cabelli, R. L. Arudi, A. B. Ross, Reactivity of HO_2/O_2^- Radicals in Aqueous Solution. *J. Phys. Chem. Ref. Data*, **1985**, 14, 1041–100.
- (S5) A. Brunmark, E. Cadenas, J. Segura-Aguilar, C. Lind, L. Ernster, DT-diaphorase-catalyzed two-electron reduction of various p-benzoquinone and 1,4-naphthoquinone epoxides. *Free Radic. Biol. Med.*, **1988**, 5, 133–43.
- (S6) J. Butler, B. M. Hoey, The apparent inhibition of superoxide dismutase activity by quinones. *J. Free Radic. Biol. Med.*, **1986**, 2, 77–81.
- (S7) Y. A. Ilan, G. Czapski, D. Meisel, One-electron transfer redox potentials of free radicals. 1. Oxygen-superoxide system. *Biochim. Biophys. Acta*, **1976**, 430, 209–24.
- (S8) Y. Song, G. R. Buettner, Thermodynamic and kinetic considerations for the reaction of semiquinone radicals to form superoxide and hydrogen peroxide. *Free Radic. Biol. Med.*, **2010**, 49, 919–62.
- (S9) J. Butler, B. M. Hoey, The apparent inhibition of superoxide dismutase activity by quinones. *J. Free Radic. Biol. Med.*, **1986**, 2, 77–81.
- (S10) I. Loeff, S. Goldstein, A. Treinin, H. Linschitz, Interactions of formate ion with triplets of anthraquinone-2-sulfonate, 1,4-naphthoquinone, benzophenone-4-carboxylate and benzophenone-4-sulfonate. *J. Phys. Chem.*, **1991**, 95, 4423–30.
- (S11) A. E. Alegría, M. López, N. Guevara, Thermodynamics of semiquinone disproportionation in aqueous buffer. *J. Chem. Soc., Faraday Trans.*, **1996**, 92, 4965–8.
- (S12) J. Baxendale, H. Hardy, The ionization constants of some hydroquinones. *Trans. Faraday Soc.*, **1953**, 49, 1140–4.
- (S13) V. Roginsky, T. Barsukova, Kinetics of oxidation of hydroquinones by molecular oxygen. Effect of superoxide dismutase. *J. Chem. Soc., Perkin Trans.*, **2000**, 2, 1575–82.
- (S14) A. Brunmark, E. Cadenas, Redox and addition chemistry of quinoid compounds and its biological implications. *Free Radic. Biol. Med.*, **1989**, 7, 435–77.
- (S15) V. A. Roginsky, L. M. Pisarenko, W. Bors, C. Michel, M. Saran, Comparative pulse radiolysis studies of alkyl- and methoxy-substituted semiquinones formed from quinones and hydroquinones. *J. Chem. Soc., Faraday Trans.*, **1998**, 94, 1835–40.
- (S16) P. Rao, E. Hayon, Ionization constants and spectral characteristics of some semiquinone radicals in aqueous solution. *J. Phys. Chem.*, **1973**, 77, 2274–6.
- (S17) X. Yuan, C. J. Miller, A. N. Pham, T. D. Waite, Kinetics and mechanism of auto- and copper-catalyzed oxidation of 1,4-naphthohydroquinone. *Free Radic. Biol. Med.*, **2014**, 71, 291–302.
- (S18) P. S. Rao, E. Hayon, Redox potentials of free radicals. IV. Superoxide and hydroperoxy radicals $^{\bullet}\text{O}_2^-$ and $^{\bullet}\text{HO}_2$, *J. Phys. Chem.*, **1975**, 79, 397–402.